



# Microstructure and Size-Dependent Mechanical Properties of Additively Manufactured 316L Stainless Steels Produced by Laser Metal Deposition

Hua-Zhen Jiang<sup>1</sup> · Qi-Sheng Chen<sup>1,2</sup> · Zheng-Yang Li<sup>1,2</sup> · Xin-Ye Chen<sup>3</sup> · Hui-Lei Sun<sup>1</sup> · Shao-Ke Yao<sup>1,2</sup> · Jia-Huiyu Fang<sup>1,2</sup> · Qi-Yun Hu<sup>1,2</sup>

Received: 8 May 2022 / Revised: 7 June 2022 / Accepted: 21 June 2022 / Published online: 16 August 2022  
© The Chinese Society for Metals (CSM) and Springer-Verlag GmbH Germany, part of Springer Nature 2022

## Abstract

Metal additive manufacturing (AM), as a disruptive technology in the field of fabricating metallic parts, has shown its ability to design component with macrostructural complexity. However, some of these functionally complex structures typically contain a wide range of feature sizes, namely, the characteristic length of elements in AM-produced components can vary from millimeter to meter-scale. The requisite for controlling performance covers nearly six orders of magnitude, from the microstructure to macro scale structure. Understanding the mechanical variation with the feature size is of critical importance for topology optimization engineers to make required design decisions. In this work, laser metal deposition (LMD) is adopted to manufacture 316L stainless steel (SS) samples. To evaluate the effect of defects and specimen size on mechanical properties of LMD-produced samples, five rectangular sample sizes which ranged from non-standard miniature size to ASTM standard sub-sized samples were machined from the block. Tensile test reveals that the mechanical properties including yield strength (YS), ultimate tensile strength (UTS), and elongation to failure ( $\epsilon_f$ ) are almost the identical for samples with ASTM standard size. Whilst, relatively lower YS and UTS values, except for  $\epsilon_f$ , are observed for samples with a miniature size compared with that of ASTM standard samples. The  $\epsilon_f$  values of LMD-produced 316L SS samples show a more complex trend with sample size, and are affected by three key influencing factors, namely, slimness ratio, cluster of pores, and occupancy location of lack of fusion defects. In general, the  $\epsilon_f$  values exhibit a decreasing trend with the increase of slimness ratio. Microstructure characterization reveals that the LMD-produced 316L samples exhibited a high stress status at low angle grain boundaries, whilst its location changed to high angle grain boundaries after plastic deformation. The grain size refinement and austenite-to-martensite phase transformation occurred during plastic deformation might be responsible for the very high YS and UTS attained in this study. The experimental works carried out in this study is expected to provide a guideline for evaluating the mechanical properties of LMD-produced parts with complex structure, where critical parameter such as a certain slimness ratio has to be considered.

**Keywords** Additive manufacturing · Laser metal deposition · 316L stainless steel · Tensile properties · Slimness ratio

Available online at <http://link.springer.com/journal/40195>.

✉ Qi-Sheng Chen  
qschen@imech.ac.cn

✉ Zheng-Yang Li  
zyli@imech.ac.cn

<sup>1</sup> Institute of Mechanics, Chinese Academy of Sciences, Beijing 100190, China

<sup>2</sup> School of Engineering Science, University of Chinese Academy of Sciences, Beijing 100190, China

<sup>3</sup> DE.Testing (JIANGSU) Co., LTD, Changzhou 213164, China

## 1 Introduction

Additive manufacturing (AM), also known as 3D printing, has been identified as one of the twelve promising technologies that constitutes the fourth industrial revolution [1]. It becomes a very attractive and promising technology for the fabrication of metallic materials because it offers many advantages over conventional methods in producing components with intricate geometry. Among many widely used AM methods, laser powder bed fusion (L-PBF, also known as selective laser melting, SLM) [2–4] and laser directed energy deposition (also known as laser metal deposition,

LMD) [5–7] are two primary AM technologies which are capable of fabricating near fully dense metallic materials for various industrial applications. It is reported that AM-produced parts can result in a hierarchically heterogeneous microstructure, with length scales spanning nearly six orders of magnitude [8]. It includes microscopic features such as melt pools, defects, crystalline grains, cellular structures, and oxide-precipitates, etc. However, significantly different microstructural sizes and metallurgical behaviors for SLM and LMD are observed because the cooling rates in the melt pool are dramatically different [9, 10]. Usually, SLM yields a finer melt pool, grain size and substructure size, while LMD yields a coarser microstructure size. Therefore, different mechanical responses may be revealed for the same materials produced by different AM technologies [9, 10].

As far as the 316L SS is concerned, the process parameters-microstructure-mechanical properties relationships of AM-produced samples have been intensively studied [2–4, 8, 9, 11–15]. Although LMD and SLM have similar capabilities and challenges, their major difference is powder delivery mechanism which influences complexity, maximum printing size, and quality of the as-deposited part. This study is interested in LMD where a feedstock material in the form of powder is delivered to a pre-processing substrate followed by a simultaneously focused laser beam, thus a melt pool is formed and a bulk material is finished after continuously depositing material layer by layer [1]. It is revealed that the UTS, YS, and  $\epsilon_f$  of LMD-produced 316L samples are in the range of 536–1050 MPa, 300–850 MPa, and 4–46%, respectively [5, 7, 9, 14, 16–19]. Such a wide range of mechanical properties observed for LMD-produced 316L SS may be attributed to the microstructure variations caused by different processing parameters as well as deposition direction. Another reason might be that the printing machines, testing conditions, and sample geometry/size are different. Recently, Gu et al. have pointed out that AM-processed parts can contain a wide range of feature sizes, for example, a crystal inspired hierarchical structure can have a characteristic scale of 0.1 mm to 10 mm during laser metal AM through structural design and innovation [20]. However, due to the dynamic nature for melting, solidification, and remelting of LMD is location dependent, the mechanical properties may vary with feature size. Therefore, investigating the size-dependent mechanical properties of LMD-produced part is of great importance to make informed design decisions.

The reported tensile property data in Refs. [5, 7, 9, 14, 16–19] showed that loading direction and processing parameters have a pronounced effect on mechanical properties of LMD-produced 316L SS samples. These studies adopted different sample geometries, namely, rectangular [5, 7, 9, 16–19] and cylindrical [14] specimens. In addition, both non-standard [5, 7, 18] and standard [9, 16, 17, 19] tensile test specimens were used to assess the mechanical

performance of the parts. The gauge length of the tensile tested samples in these studies ranged from 9 to 40 mm while the gauge width of the samples was 2.5 mm–10 mm. The main advantage of using non-standard miniature specimens is that it can capture and mimic the location-dependent mechanical properties in LMD-produced samples, whilst a large standard tensile specimen might not capture the spatial variations [21, 22]. However, unlike materials prepared by traditional methods such as die castings, the quality of specimens can be evaluated by a standard sample geometry and size. There is currently no standard available for qualifying the mechanical properties of AM-produced specimens. Research to date has identified that the inevitably formed defects could substantially undermine the mechanical properties of LMD-produced samples. These critical defects such as pores and lack of fusion are still a universal problem for LMD-produced parts [22]. The adverse effect of these defects may become more prominent with decreasing specimen size [22, 23]. However, most of the studies carried out investigating the size dependency tensile properties are mainly focused on PBF-produced materials especially for Ti6Al4V [21, 23–26], it is not yet understood how tensile properties of LMD-produced 316L SS vary with specimen size. More importantly, the LMD-produced 316L SS samples appear more brittle features because the sizes of substructure, defects, and oxide inclusions are significantly larger than that of SLM [4, 9, 27]. Therefore, the mechanical properties of LMD-produced 316L samples may be highly related to specimen size especially for the elongation of the material. While, the details of the size dependency tensile properties of LMD-produced 316L SS are not well documented and worth thorough investigations. In this regard, 316L SS was manufactured in this work as a studying case to understand the effect of defects and sample size on the mechanical properties of LMD-produced samples. The microstructure, represented fracture surfaces, and possible fracture mechanism are presented and discussed based on the experimental results from this study and those in literature.

## 2 Materials and Methods

### 2.1 Materials

As received gas-atomized 316L spherical powders with particle sizes ranging from 50 to 150  $\mu\text{m}$  were purchased from Tianjin Zhujin Technology Development Corporation, China (Fig. 1a). The chemical compositions of the powder by weight were characterized by energy-dispersive X-ray spectroscopy (EDS) and the results are listed in Table 1. The reported values are averaged from two measurements. As can be seen in the figure, the as-used powders are spherical in shape with rather smooth surfaces and exhibit the

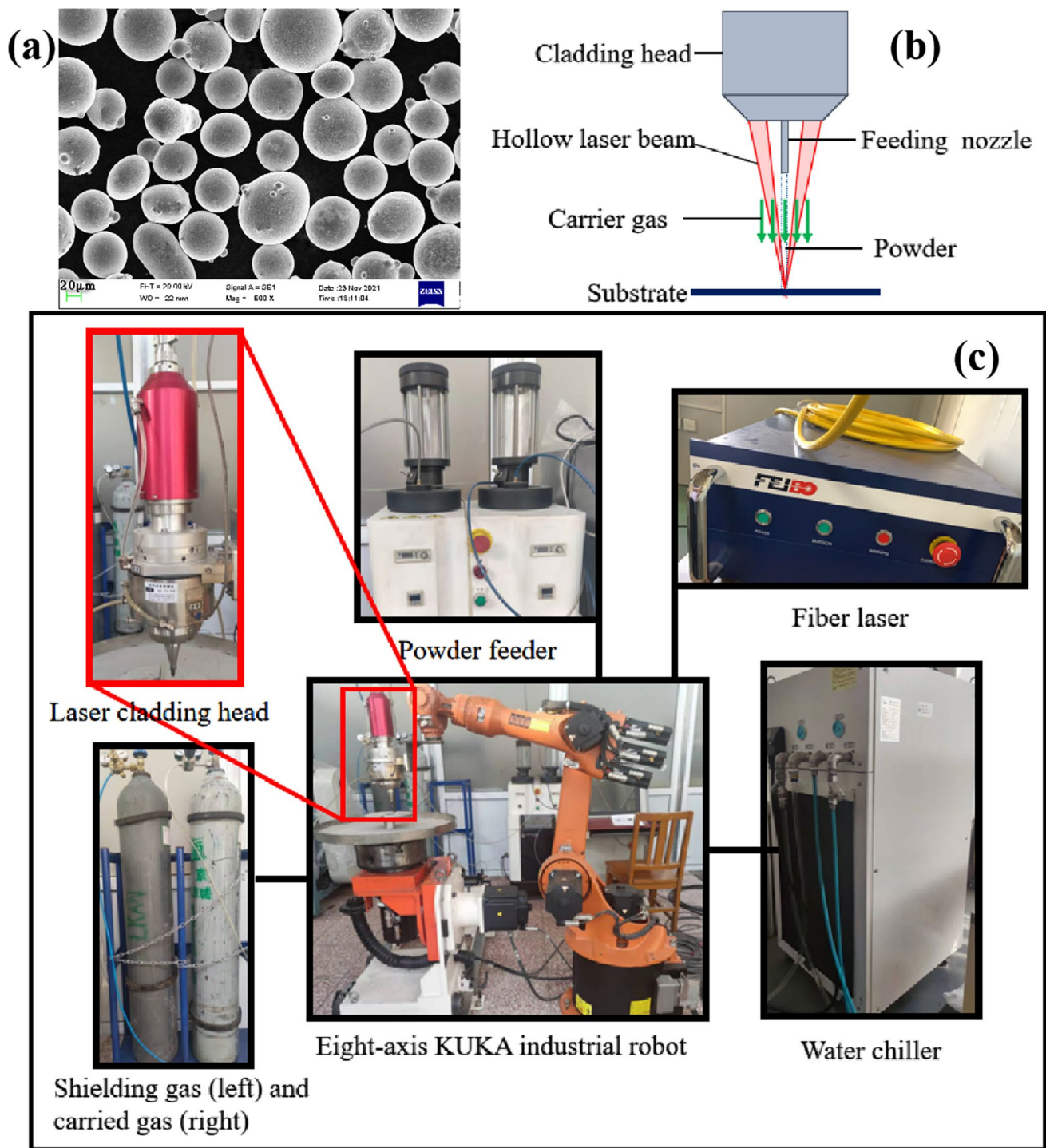


**Fig. 1** Experimental details in the study: **a** morphology of the as-used 316L SS powder, **b** a sketch of laser inside powder feeding nozzle, and **c** real photograph of the LMD system

**Table 1** Chemical composition of as-used 316L SS powders (wt%)

Fe	Cr	Ni	Mo	Mn	Si	C	P	S
Bal.	19.30±0.5	11.15±0.65	1.70±0.2	0.60±0.3	1.40±0.1	≤0.03	≤0.04	≤0.01

satellites which are a typical defect that can be formed in the gas atomized powders.

## 2.2 Experimental

The deposition system used in the present work is shown in Fig. 1c. It consists of a six-axes robot (KR16, Kuka, Germany), a two-axes rotation positioner, a diode fiber laser system YDFL-2000-CW-MM (Shanghai Feibo Laser Technologies Co., Ltd) with a wavelength of 1080 nm, a metal powder feeder (RC-PGF-D-2, Raycham, China), a water chiller (TFLW-1000WDR, Tongfei, China), and a laser cladding head. The principle of the special designed laser inside powder feeding nozzle was sketched in Fig. 1b. A hollow laser beam was obtained by using the cone mirror to split the input solid laser beam, and thus the energy intensity of the hollow laser beam was regulated along the radial direction to get a saddle-hacked distribution. Readers may refer to Ref [28]. for more detailed information. The 316L SS plate with a dimension of 150 mm × 150 mm × 15 mm was used as the substrate material. Prior to the deposition, the plate surface was polished and then cleaned by 75% alcoholic solution. Argon with 99.99% purity was chosen as the shielding and carrier gas to avoid oxidation of the melt pool and feed powders during deposition (Fig. 1c). The Taguchi method [2, 29], a powerful tool to design optimization for quality, is used to find the optimal laser process parameters for the manufacturing process. An orthogonal array based on  $L_9$  Taguchi matrix is employed and the micro-hardness of each LMD-produced sample was chosen as a response variable to assess the resultant quality. Since the focus of this study is not to optimize the laser process parameters, hence, we presented the details of optimization for hardness in Supplementary Materials Appendix A for clarity and completeness. The optimized laser process parameters are listed in Table 2.

The laser beam was defocused to give a spot diameter of 2 mm. When injected powders were fed into the melt pool created by the laser beam, a deposited layer was subsequently formed followed by rapid solidification. Self-developed slicing software called “3dAM-PP-Planner” was used to help design the deposition path. To control the shape precision and the surface morphology of the samples, the variation-orientation raster scanning strategy used in Ref. [30] was adopted to fabricate the parts in this work. The starting point of each layer is random with the angle of the laser

rotated by 105° between each layer. In order to study the influence of the different specimen sizes on the mechanical properties of LMD-produced parts, a block with a dimension of 110 mm × 80 mm × 15 mm was manufactured by using the optimized laser process parameters listed in Table 2. Thereafter, five different part sizes ranging from miniature size to ASTM E8 sub-sized were machined by wire cutting from the block. The designed five different sample geometries are detailed in Fig. 2a–e.

## 2.3 Details of Microstructural and Mechanical Characterization

The top surface of the block was milled to remove 1.5 mm of the deposited layer. For microstructural characterizations, a cuboid sample with a dimension of 10 mm × 10 mm × 2 mm was machined from the block. Thereafter, the cuboid sample was sectioned and its top surface was used for microstructure observation (Fig. 2f, TD-LD plane, perpendicular to the build direction). A mirror like surface was achieved by using a standard metallography procedure detailed in Ref. [3]. The relative density of the part (in percentage) was analyzed using the Image-Pro Plus 6.0 software under optical microscopy (OM, VHX-5000). This method evaluated the sample's porosity by counting the area percentage of pores on the polished surface [3]. Afterwards, polished surfaces were electrolytically etched by using a solution of 10% oxalic acid at 6 V during 20 s. The LMD-produced and deformed samples were then observed through OM and scanning electron microscopy (SEM, ZEISS). An extra step of oxide polishing suspensions (OPS) polishing was performed to prepare the samples for the electron backscattered diffraction (EBSD, EOL JSM-7900F) observation. All observed specimens were tilted to 70° in the SEM chamber at an accelerating voltage of 20 kV. The observation for as-built sample was carried out at the position near the middle of the polished surface (Fig. 2f), whilst deformed sample was observed near the fracture site. The step sizes used for LMD-produced and deformed samples were 2 μm and 1.4 μm, respectively. Data analysis was performed with the TSL-OIM analysis software. For statistics, any pair of indexed points with misorientation exceeding 2° is considered a boundary. The low angle grain boundary (LAGB) is defined as misorientation < 10°, while the misorientations over than 10° are referred to as high angle grain boundaries (HAGBs) [8, 31]. The pole figure (PF) was computed by a harmonic series expansion method and a Gaussian smoothing of 5°. The kernel average misorientation (KAM) map was calculated from the EBSD data on the same cross-section with an upper threshold of 5°, above which any misorientations are excluded in the calculation. In addition, EDS analyses were carried out on some spherical particles

**Table 2** Optimal process parameters used in this work

Laser power (W)	Beam diameter (mm)	Scanning speed (mm/s)	Powder feeding rate (g/min)	Hatch spacing (mm)	Layer thickness (mm)
1100	2.0	6.0	10.3	1.0	0.2



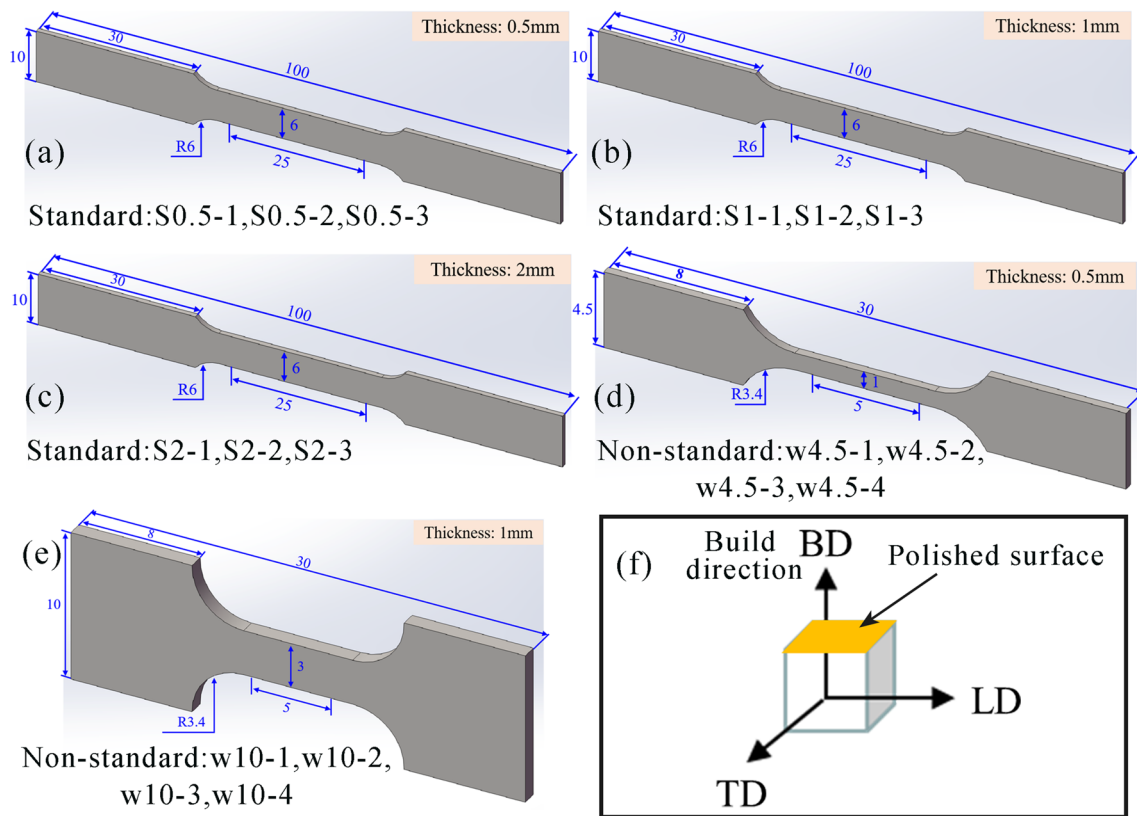


**Fig. 2** a–e Detailed information about specimen geometries, f polished surface used for microstructural observation

in some fractured surfaces in order to investigate their possible oxidation behaviors.

## 2.4 Test of Mechanical Properties

All the side surfaces of the machined tensile specimens were manually ground by using SiC papers to remove the deformed layer that may generate during the wire cutting process. Tensile tests were then performed at room temperature on an electronic universal testing machine (UTM5105X, SANS) with a strain rate of  $3.33 \times 10^{-3} \text{ s}^{-1}$ . The strength calculations were performed using measured gauge width and sample thicknesses. Three repetitions were conducted for the standard specimens, whereas four repetitions were conducted for the non-standard specimens. For the convenience of subsequent analysis, we have named these specimens and the corresponding sample numbers are depicted in Fig. 2a–e. A 5 kN load cell was used for Samples ‘w4.5’ and Samples ‘w10’, whilst a 100 kN load cell was utilized for Samples ‘S0.5’, Samples ‘S1’, and Samples ‘S2’. A powerful non-contacting deformation measurement system (i.e., Vic-3D LS) was applied to measure the tensile strain of the tested samples. All the tests were conducted until fracture occurred. The YS, UTS, and  $\epsilon_f$  values were obtained from the corresponding engineering stress–strain curves. After

tensile test, some typical fracture surfaces were inspected by SEM.

## 3 Results and Discussion

### 3.1 Microstructure

Figure 3a depicts the typical defects generated in LMD-produced sample. The corresponding defect size distribution is displayed in Fig. 3b. It is observed that the majority of defects are usually less than  $50 \mu\text{m}$  and the distribution of these defects is not uniform. In some local areas, lack of fusion defect with size greater than  $50 \mu\text{m}$  was observed (see Supplementary Materials, Appendix B). An area around  $6.4 \text{ mm}^2$  was analyzed and the relative density of sample was measured to be  $(99.19 \pm 0.76) \%$ . This value is comparable to a SLM-produced part, which relative density greater than 99% is usually assumed to be high-density part [3, 8, 13, 32]. The LMD-produced sample is characterized by a mixture of columnar dendrites and cellular structures as revealed by OM and SEM images shown in Fig. 3c–e. The fraction of the dendrites and cells in arbitrary regions of the sample is roughly estimated using Image-Pro Plus 6.0 software, and the result is 86.6% and 13.4%, respectively. The

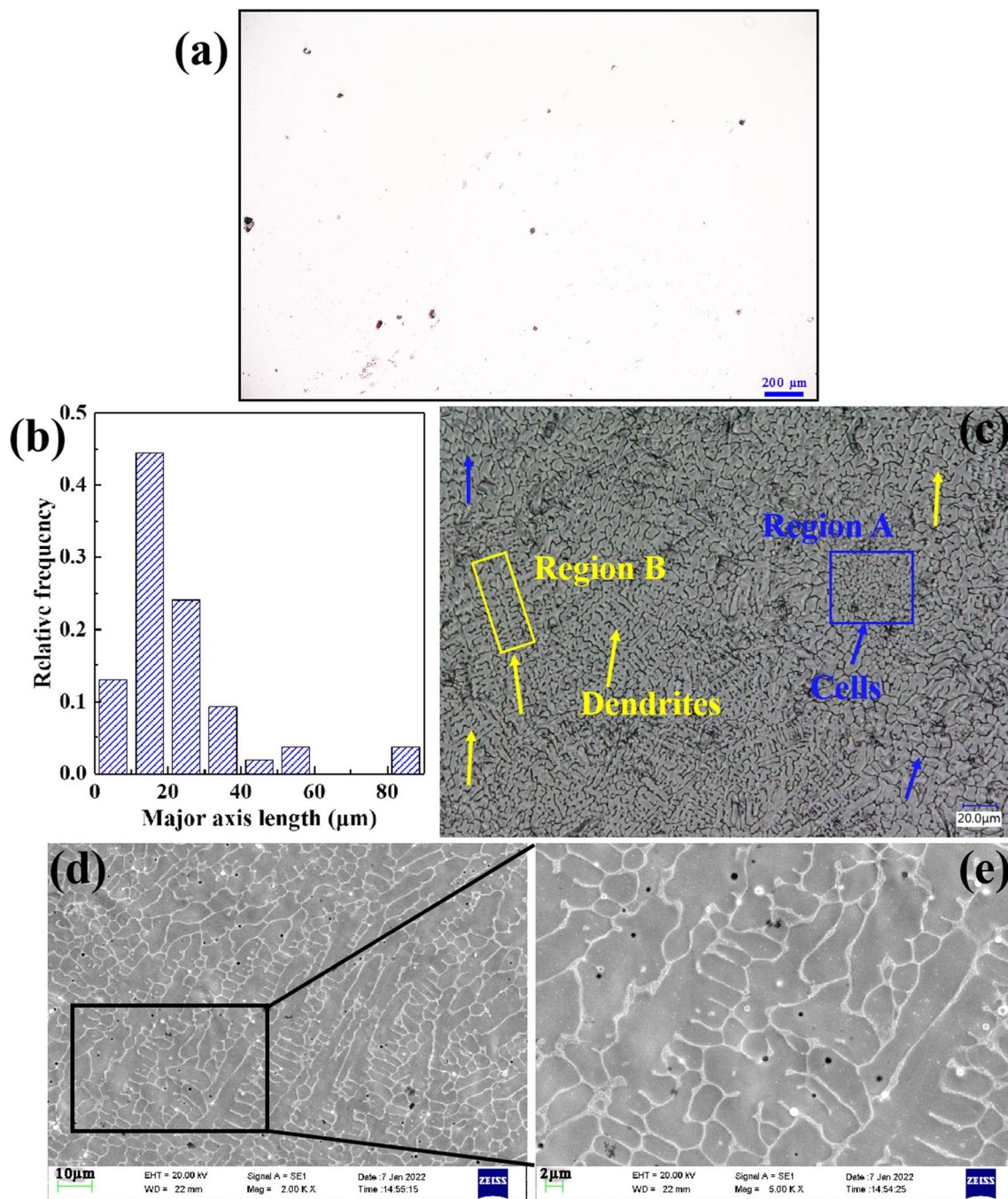


**Fig. 3** **a** Defects detection using OM method, **b** the corresponding distribution of defect size in terms of the major axis length in **a**, **c** OM image showing the columnar dendrites (e.g., region B) and cells (e.g., region A) in the material, the yellow and blue arrows indicate dendrites and cells, respectively, **d** SEM image revealing the solidification microstructure, **e** a magnified view showing the columnar dendrite and cell structures

phenomenon is in accord with the observation reported in Refs. [18, 19], in which the dendrites are a major structure in a LMD-produced 316L sample. Depending on the location within the melt pool, various shapes and sizes of the structures can be observed. Previous studies reported that critical parameters such as the temperature gradient  $G$ , solidification rate  $R$  are the key to determining the microstructure of such

an alloy produced by LMD [33]. The ratio  $G/R$  determines the mode of solidification while the product  $G \cdot R$  governs the size of the solidification microstructure [33]. To explain the complex microstructures observed in this study, we selected two typical areas in Fig. 3c for quantitative analysis. The two analyzed structures, i.e., cells and dendrites, are marked by blue and yellow rectangle, respectively. The corresponding

$G$  and  $R$  values were estimated and the detailed information was presented in Supplementary Materials Appendix C. The calculated cooling rate in region A is  $1.75 \times 10^4$  K/s, which is significantly higher than that of region B (the value is  $2.38 \times 10^3$  K/s). Therefore, a relatively finer structure was observed in region A. In addition, the estimated  $G/R$  values in region A and region B are  $1.28 \times 10^3$  K s/mm<sup>2</sup> and  $1.75 \times 10^2$  K s/mm<sup>2</sup>, respectively. According to the solidification map constructed by  $G$  and  $R$ , the solidification microstructures can change from cells to columnar dendrites with decreasing  $G/R$  values [33], and our experimental observation evidenced this phenomenon (see Fig. 3c, region A and region B). Therefore, it is reasonable to speculate that local change in  $G$  and  $R$  values result in the formation of microstructures with different shapes and sizes [34] (see Fig. 3c–e). The secondary arm spacing or cell size is estimated to be 2–5  $\mu$ m, and the length of dendrite is a few tens of microns, which are the typical microstructural length scales of LMD-produced 316L SS reported in the literature [35]. The image quality (IQ) map, inverse pole figure (IPF) image, pole figure (PF), band contrast map, KAM distribution image, and phase map of the sample are all presented in Fig. 4a–f. Note that the IPF map together with its corresponding PF map is calculated from EBSD data with respect to the build direction. The corresponding misorientation angle distribution and grain size distribution are displayed in Fig. 4g–h. It can be seen from the IPF map that the grains of LMD-produced sample is quite irregular, and both equiaxed and elongated columnar grains can be seen from the image. This is very different from a wrought 316L in which the microstructure is fully equiaxed and is uniformly distributed (see Supplementary Materials, Appendix D). The average grain size of LMD-produced sample is around 38.29  $\mu$ m (Fig. 4h). The three colors (i.e., red, green and blue) in the IPF orientation map indicates alignment of  $\langle 001 \rangle$ ,  $\langle 101 \rangle$  and  $\langle 111 \rangle$  axes with the build direction [36, 37]. Hence, grains with the same crystallographic orientation have similar colors. It can be seen from Fig. 4b that the grains are mainly dominated by red and green colors, suggesting that multicomponent cubic textures may be formed. This is evidenced by pole figures shown in Fig. 4c because the highest pole densities in the  $\{001\}$  and  $\{101\}$  pole figures at specific  $\{001\}$  and  $\{101\}$  positions are basically consistent with the standard stereographic projection. The KAM value generally can be reflected to geometrically necessary dislocations (GND) and can be used to indicate the stress status of the sample. A larger KAM value at a specific location in KAM map suggests a relatively higher stress status [38]. Compared with wrought 316L, the LMD-produced part exhibited a very high stress status (see Fig. 4e and Supplementary Materials, Appendix D). This is believed to be correlated with the high density of dislocations during the rapid solidification for additive manufactured part [38, 39]. The percentage of

LAGBs for the LMD-produced sample is 38.7% (Fig. 4g), which is lower than the reported values for a SLM-manufactured 316L SS (the values are in the range between 41 and 87% [8, 31, 32, 36]). Previous studies have revealed that LAGB is a kind of dendrite cell boundary and is enriched of dislocation for a SLM-produced 316L SS [12, 40]. This is also evidenced by the KAM mapping and band contrast map that the high stress status is usually located at LAGBs (see Fig. 4d–e). In addition, the LMD-produced sample consists of fully face-centered-cubic (FCC)  $\gamma$  austenite phase with no  $\delta$  ferrite detected, as revealed by EBSD phase mapping shown in Fig. 4f. The result is in line with the works carried out in literature [35, 41, 42] where no ferrite peaks could be located on the X-ray diffraction intensity versus  $2\theta$  plots. It should be noted that some researchers also reported the presence of a small amount of  $\delta$  ferrite for a LMD-produced 316L SS [17, 27, 37]. The  $\text{Cr}_{\text{eq}}/\text{Ni}_{\text{eq}}$  ratio and cooling rate might be responsible for the different results observed in the literature and have been sufficiently discussed in the previous works [19, 27]. In fact, Elmer et al. [43] pointed out that stainless steel alloys can only solidify within the single phase austenite mode due to the suppression of solute redistribution at a high cooling rate. Therefore, higher cooling rate in this study may be responsible for the observed fully austenitic microstructure.

### 3.2 Effect of Defects and Sample Size on Mechanical Properties

To better understand the effect of defects and sample size on the tensile properties of LMD-produced 316L SS samples, five different part sizes ranging from miniature size to ASTM E8 sub-sized were tested, and the results are depicted in Fig. 5. The UTS, YS, and  $\epsilon_f$  are all presented. It shows that the average YS values are in the range between 660 and 741 MPa, whereas average UTS values are in the range between 879 and 938 MPa. The tensile yield strength and ultimate tensile strength of LMD-produced samples are much higher than that of the forged part (the values of YS and UTS for wrought 316L are 220–345 MPa and 520–680 MPa, respectively [44–47]). However, significantly lower  $\epsilon_f$  values are obtained for the LMD-produced specimens compared to that of the forged counterpart (the value is between 30 and 55% [44–47]). The reason for the peculiar mechanical properties of LMD-produced 316L samples is ascribed to their unique microstructure [11]. It can be seen here that the tensile properties including YS, UTS, and  $\epsilon_f$  are almost the identical for samples with ASTM E8 size, especially considering their standard deviation (Fig. 5a–c, Samples ‘S0.5’, ‘S1’, and ‘S2’). However, the YS and UTS values for samples with miniature sizes (i.e., Samples ‘w4.5’ and ‘w10’) generally show a slightly decreasing trend when compared with that of ASTM E8 samples (Fig. 5a and b).



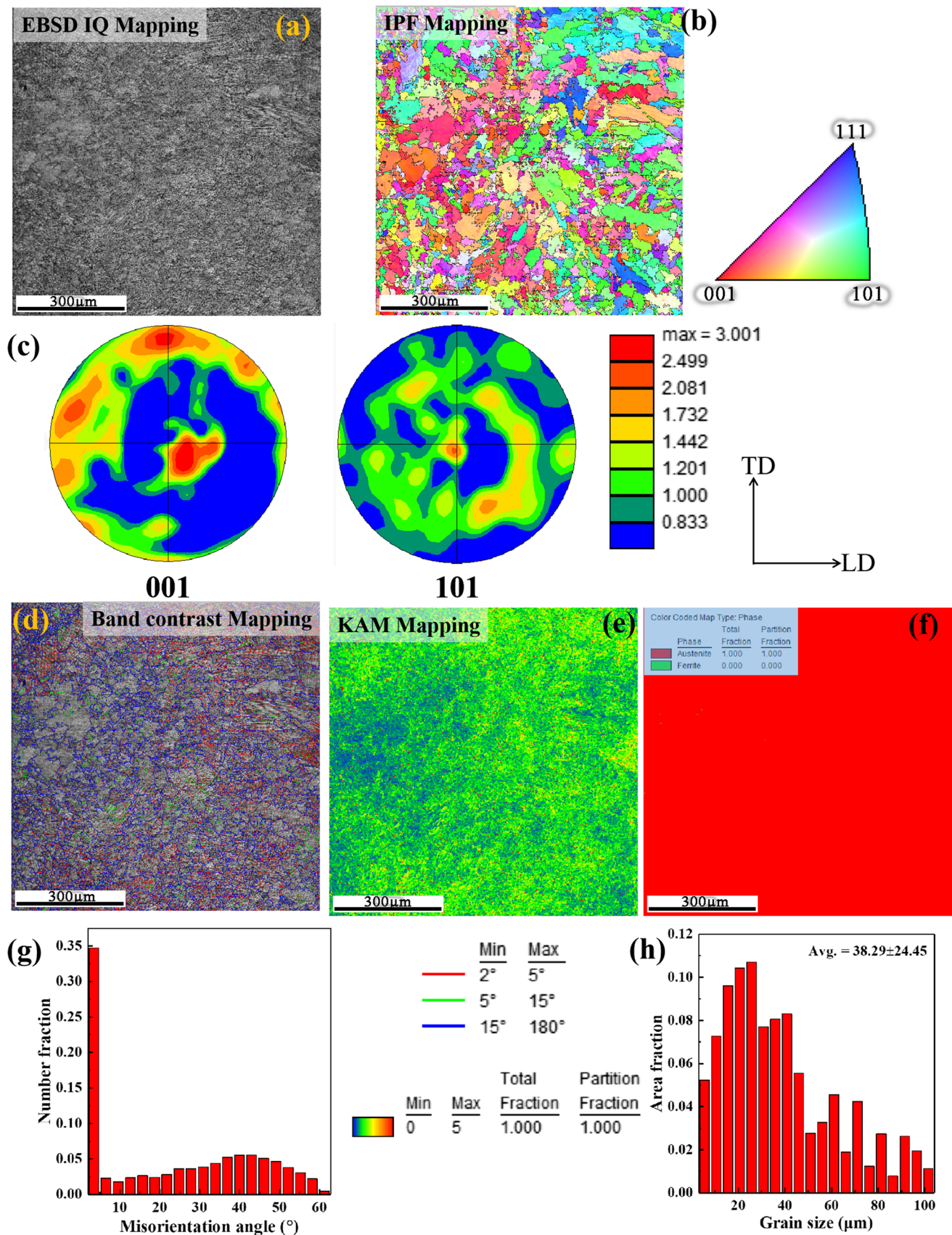




**Fig. 4** Microstructure of LMD-produced 316L SS sample observed by EBSD: **a** IQ map, **b** IPF image, **c** PF image, **d** band contrast map, **e** KAM map, **f** phase mapping, **g** misorientation angle distribution, and **h** grain size distribution

This phenomenon was also reported for L-PBF produced 304L and Ti6Al4V samples, namely, the YS and UTS values exhibit a decreasing trend below a critical sample thickness [23, 25]. In addition, it is noticed that larger standard deviation for YS, UTS, and  $\epsilon_f$  is observed for samples with miniature size (Samples ‘w4.5’ and ‘w10’). This is believed to be caused by both the measured uncertainties and increasing importance of contribution from the probability of the presence of built-in flaws and their influence [22]. The effect of built-in flaws which is inevitably formed in LMD-produced sample will be accentuated for the small size sample. Nevertheless, the elongation to failure exhibited a more complex trend since the highest value of  $\epsilon_f$  was obtained in miniature size samples, namely, Sample ‘w10’, although a highest standard deviation was observed in these specimens (Fig. 5c). In general, the values of  $\epsilon_f$  for miniature size samples are greater than that of samples with ASTM E8 size. The result challenges previous viewpoint that the elongation to failure of PBF-produced Ti-6Al-4 V samples decreases continuously as the sample thickness decreases [26]. Actually, Davis [48] have pointed out that elongation of a material is affected by test-piece geometry including gage length, width, and thickness of the gage section. Hence, comparing elongation values accordingly to different sample geometries by just using sample thickness may be not scientifically enough. According to the well-established Bertella-Oliver equation, elongation of a material is influenced by the slimness ratio [48]. It is defined as the gage length divided by the square root of the cross-sectional area of the specimen. Here, we plotted the elongation of parts versus the slimness ratio, and the results are displayed in Fig. 5d. Overall, the values of elongation to failure show a decreasing trend with the increase of slimness ratio. The tendency is consistent with the conventionally manufactured steels [48] and also in line with PBF-produced Ti-6Al-4 V samples [22]. Interestingly, we observed that the  $\epsilon_f$  value of Sample ‘w4.5’ was slightly larger than that of Sample ‘S1’ although their values of slimness ratio are very close to each other. Therefore, the inevitably microstructural features in LMD-produced samples, namely, the presence of lack of fusion and internal pores may also play a significant role in determining the ductility of LMD-produced parts. The following will discuss it through inspection of their fracture surfaces by SEM for samples with low and high  $\epsilon_f$  values.

Figures 6, 7, 8, 9, 10, 11 show the representative macro fracture surfaces and some enlarged areas for Sample ‘S0.5–1’, Sample ‘S1–1’, Sample ‘S2–2’, Sample ‘w4.5–4’, Sample ‘w10–4’, and Sample ‘w10–1’, respectively. The total

elongation of Sample ‘w10–1’ is the highest among all of the tested samples and is inspected for a comparison purpose. Whilst the other samples observed have the lowest  $\epsilon_f$  value at the specific sample size, i.e., Sample ‘S1–1’ is observed because its  $\epsilon_f$  value is the lowest among Samples ‘S1–1’, ‘S1–2’, and ‘S1–3’, and so on. The corresponding defect size distribution and area fraction of defect region measured on these fracture surfaces are presented in Fig. 12. As shown in Figs. 6, 7, 8, 9, 10, 11, the fracture surfaces are characterized by built-in flaws such as pores and lack of fusion defects. In these figures, the blue arrows indicate pore defects whereas the yellow dotted rectangles are used to mark lack of fusion defects. For the former case, the sizes of pores are usually less than 50  $\mu\text{m}$  and are spherical in shape. Whilst, for latter, the defects are irregular and are strip-like in shape with its size greater than 50  $\mu\text{m}$  (see Fig. 12). Obviously, the variation of  $\epsilon_f$  value is attributed to not only the sample geometry (Fig. 5d), but also the distribution of pores and occupancy location of lack of fusion defects (Figs. 6, 7, 8, 9, 10, 11). The presence of these defects can act as stress amplifier and aid in crack propagation during tensile test. This is evidenced by Fig. 13a and b where the crack initiates from a residual pore or the crack propagates to the edge of the sample surface. According to the theory of fracture mechanics, the stress concentration coefficient of a lack of fusion defect (irregular shape with edges or corners) is larger than that of a pore (usually with a spherical shape). Therefore, it is vital to avoid the lack of fusion defects so as to improve the mechanical property of the part. Figure 8 shows that the fracture was initiated from large size of the strip-like lack of fusion defects (Sample ‘S2–2’). These defects are located at the edge of the sample surface and the length of the defects can be as large as 1015  $\mu\text{m}$ . A total area fraction of defect  $\sim 1.26\%$  was measured which is higher than that of others except Sample ‘w4.5–4’ (see Fig. 12b). The crack initiated from the large size of lack of fusion defects and propagated to the sample’s exterior surface, resulting in a lowest value of total elongation to failure ( $\epsilon_f = 11.7\%$ ). Two obvious lack of fusion defects were also observed in Sample ‘w10–4’ and these defects were situated at the edges of the sample, hence a relatively lower total elongation value, i.e., 15.7%, was obtained (Figs. 10 and 12). Compared with Sample ‘S2–2’ and Sample ‘w10–4’, the rest of inspected fracture surfaces contained relatively fewer lack of fusion defects and its size was also smaller (Figs. 6, 7, 9 and 12). However, relatively lower values of total elongation to failure were also observed in the rest of samples except Sample ‘w10–1’. The cluster of pores also had a significant impact on premature failure of LMD-produced samples (Figs. 6, 7, 9 and 10). We observed two key influencing factors that may deteriorate elongation of LMD-produced 316L samples. One is too many small pores are occupied on the fracture surfaces. The characteristic lengths of these kinds of pores are usually less than

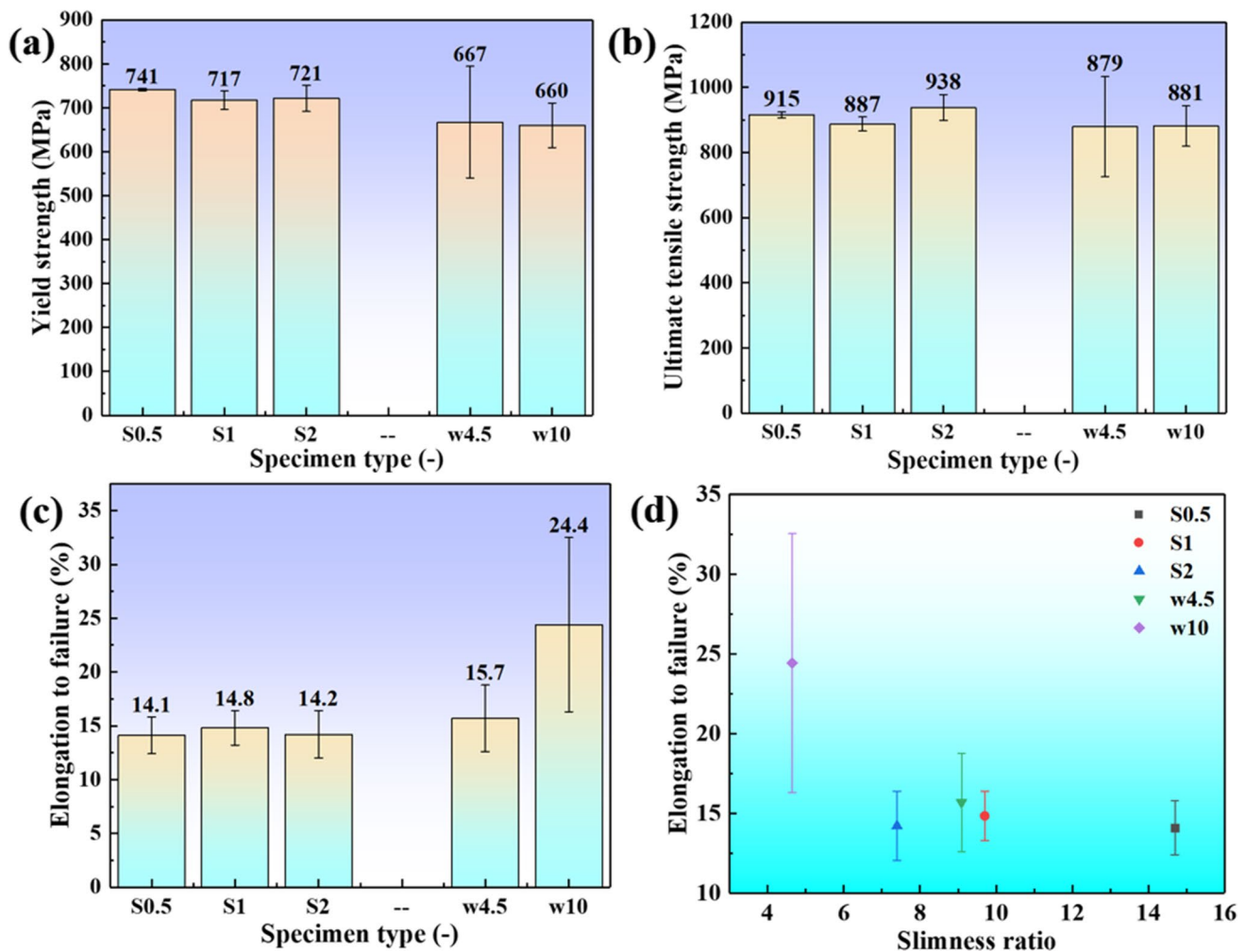


**Fig. 5** A summary of mechanical properties versus specimen size for LMD-produced 316L SS samples: **a** yield strength, **b** ultimate tensile strength, **c** elongation to failure, and **d** slimness ratio dependence of elongation to failure with different specimen sizes

50  $\mu\text{m}$  and situated at the edges or subsurface of the samples (see Figs. 6, 7a–b and 12). The other is pores are relatively large compared to the cross-section of the sample. As shown in Fig. 9a, two large pores with diameters around 88  $\mu\text{m}$  and 121  $\mu\text{m}$  were observed near the center of the fracture surface. The measured total pore area fraction is 1.81% which is the highest among all of the tested samples (Fig. 12). These pores can not only act as a stress amplifier which in turn accelerated crack propagation during tensile loading, but also cause a reduction of effective cross-sectional area, both of which are adverse to sample total elongation to failure. In contrast, Sample ‘w10-1’ had relatively smaller sized lack of fusion defects at the edges, and the stochastically distributed pores in the sample were both small in size and in quantity, resulting in a highest value of total elongation to failure among all of the tensile tested samples ( $\epsilon_f=35\%$ , Figs. 11 and 12). Note that the value of slimness ratio for Sample ‘w10-1’ is the lowest among all the tested samples.

A highest  $\epsilon_f$  was obtained for Sample ‘w10-1’ although the area fraction of defects was relatively higher than that of Samples ‘S0.5-1’ and ‘S1-1’. Therefore, it concluded that the highest  $\epsilon_f$  value is the combination of smaller slimness ratio (i.e., geometry effect) and with fewer defects. The above analyzed results indicated that there may be at least 2 different conditions resulting in the premature failure of the specimen. One is large size of lack of fusion defects situated at the edges of the samples, such as Sample ‘2-2’ and Sample ‘w10-4’. The other is big pores or cluster of pores reduced the effective cross-section area of LMD-produced samples, such as Samples ‘S0.5-1’, ‘S1-1’, and ‘w4.5-4’. However, at a high magnification, all fracture surfaces are characterized by fine dimples with a size comparable to the dendrite arm spacing or cell size (Figs. 6, 7, 8d, 9, 10c, and 11d). Zhong et al. [4] have pointed out that the detachments of cellular substructure for a SLM-produced 316L SS sample form the ductile dimples on the tensile fracture surface, and

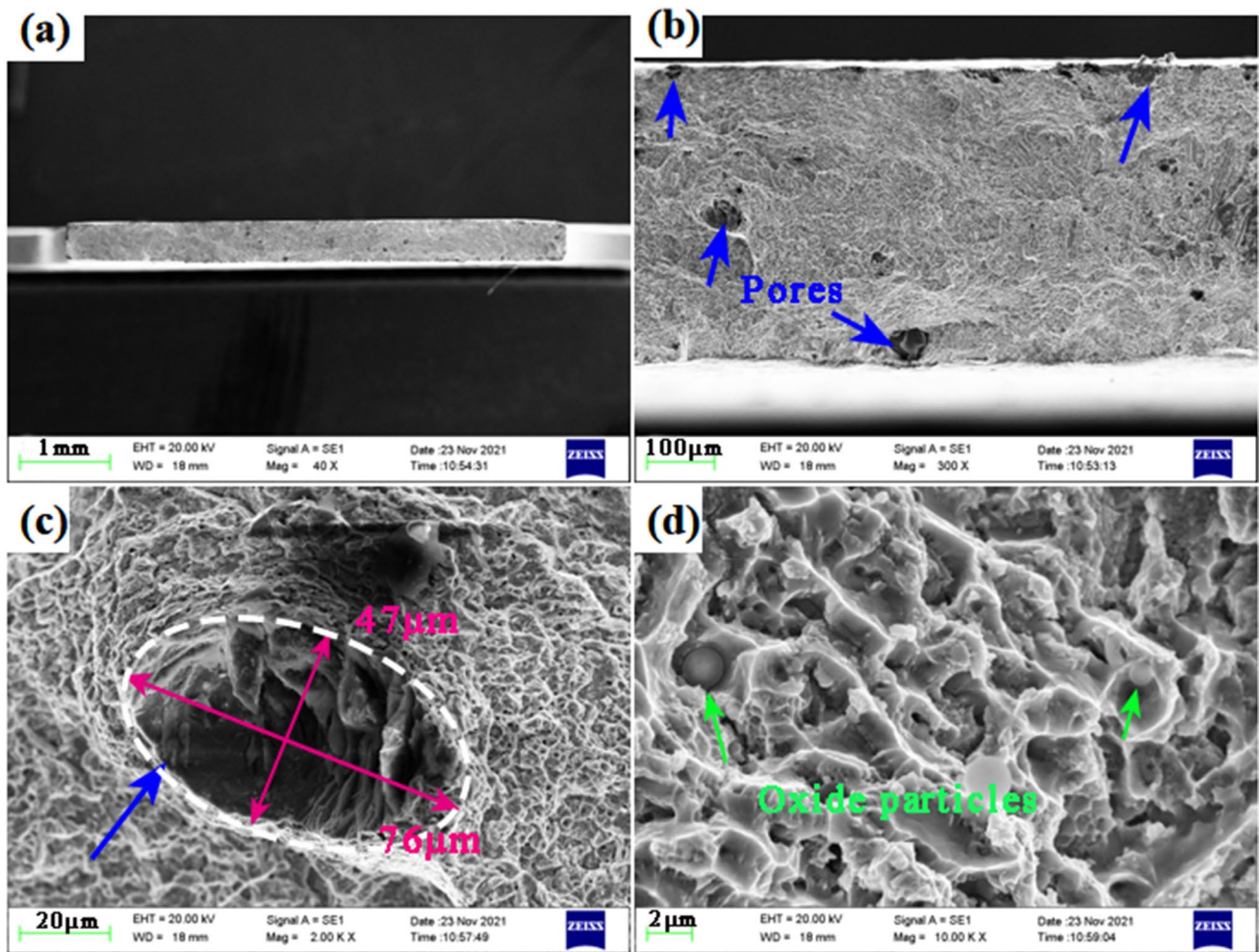


**Fig. 6** Represented fracture surface of sample ‘S0.5–1’ ( $\epsilon_f = 12.9\%$ ). **a** Macroscopic fracture morphology, **b**, **c** are enlarged images showing the pore defects, **d** a high magnified image revealing the dimple fracture and oxide particles

this is the reason why the sizes of dimples are constrained to cell size of the part. Therefore, it is reasonable to speculate that the substructure of LMD-produced sample may also play an important role in determining the size of dimples. It should be noted that the dimple size of LMD-produced 316L sample is an order of magnitude larger than that of SLM, and this is one of the reasons why the ductility of a LMD-produced sample is lower compared with that of SLM.

Another possible reason for the observed low total elongation to failure for LMD-produced samples in the study may be attributed to formation of oxide particles (see Figs. 6, 7, 8, 9, 10, 11, the green arrows indicate oxide particles). The oxidation behavior is a common phenomenon in LMD-produced 316L sample and is difficult to eliminate [15, 17, 27]. This is because LMD process is usually conducted in open environment and shielding gas such as argon is adopted to prevent local oxidation of materials. The high affinity of Si/Mn element to oxygen at high temperature results in the formation of oxide particles [27, 49]. It

should be highlighted that oxide particles are also reported in a SLM-produced 316L sample even though the oxygen content in the build chamber is less than 1000 ppm [4, 8]. To indicate the chemical composition of oxide inclusions and LMD-produced 316L base material, EDS was performed on various sample fracture surfaces. The average results are listed in Table 3. It can be observed that these oxide inclusions are rich in Si or Si/Mn compared to the LMD-produced base material. The result is consistent with the works carried out in the literature [15, 17, 27]. The formation of these oxide particles can change the failure behavior of a sample from ductile to brittle mode. This is because these oxides could decrease the maximum capacity of material to be plastically deformed [27]. As a result, the elongation to failure of the sample is decreased. It should be highlighted that some researchers also concluded that the formed oxide nano-inclusions in a SLM-produced sample could strengthen the material properties [4, 49]. However, recent works using Orowan strengthening model [8] and Russel-Brown model



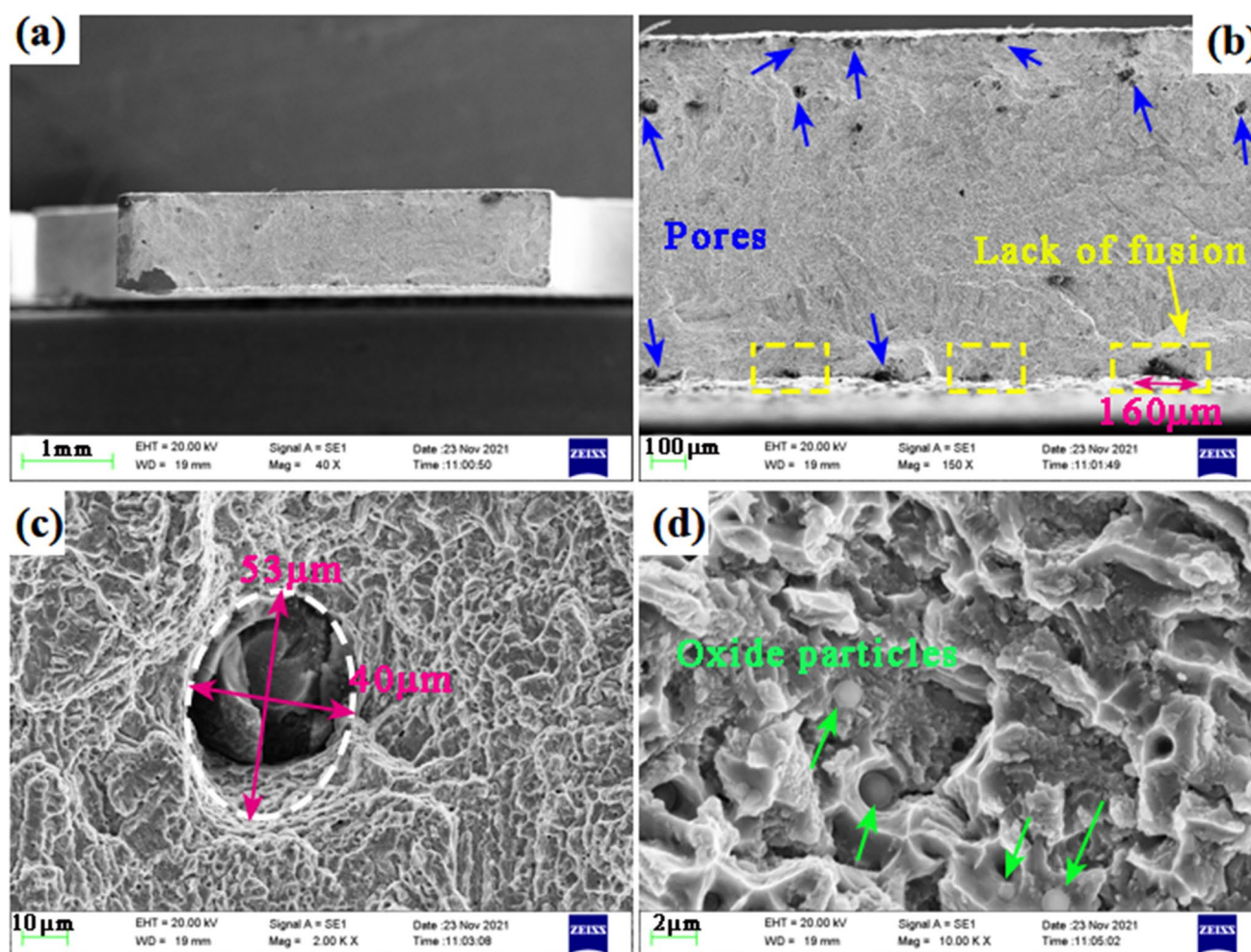


**Fig. 7** Represented fracture surface of sample 'S1-1' ( $\epsilon_f=14.2\%$ ). **a** Macroscopic fracture morphology, **b**, **c** are enlarged images showing the pores and lack of fusion defects, **d** a high magnified image revealing the dimple fracture and oxide particles

[50] revealed that the oxide strengthening effect is negligible. According to the Orowan strengthening mechanism [8, 50], a smaller oxide particle yields a higher strengthening effect. For a LMD-produced sample, the sizes of the oxide particles are usually larger than 300 nm (Figs. 6, 7, 8d, 9, 10c, and 11d), which is substantially greater than that of SLM (the size is usually less than 100 nm [8, 50]). Therefore, the strength contribution effect from oxide particles for a LMD-produced 316L sample may also be negligibly small. Moreover, the oxide particles are dispersed randomly in the fabricated samples due to the distribution of these oxide particles are not a controlled processing process. Hence, the non-uniformly distributed oxides should have a very limited strengthening effect in LMD-produced 316L samples. Recently, Saboori et al. [17, 27] have pointed out that the presence of these oxide particles in LMD-produced samples does not have any strengthening effect, and it plays a detrimental role in mechanical properties especially for the elongation of a material. Further work should be carried out

to reduce the content of oxide particles but is not the focus of this study.

Although various types of defects have been revealed by SEM through the inspection of fracture surfaces for LMD-produced 316L samples, very high YS and UTS values are still achieved in this study (Fig. 5). Here, we compared our experimental results with the reported LMD-produced 316L SS data from the literature (including rectangular and round specimens), and the results are depicted in Fig. 14. It is observed that most of the studies conducted were using rectangular tensile specimens, and non-standard tensile specimen dimensions were also adopted to evaluate the mechanical properties of the LMD-produced 316L SS samples (see Supplementary Materials, Appendix E). A classical strength-ductility tradeoff behavior for such an alloy produced by LMD is clearly revealed. This behavior is very different from a SLM-produced 316L (see Supplementary Materials, Appendix E), which the strength and ductility could be simultaneously enhanced



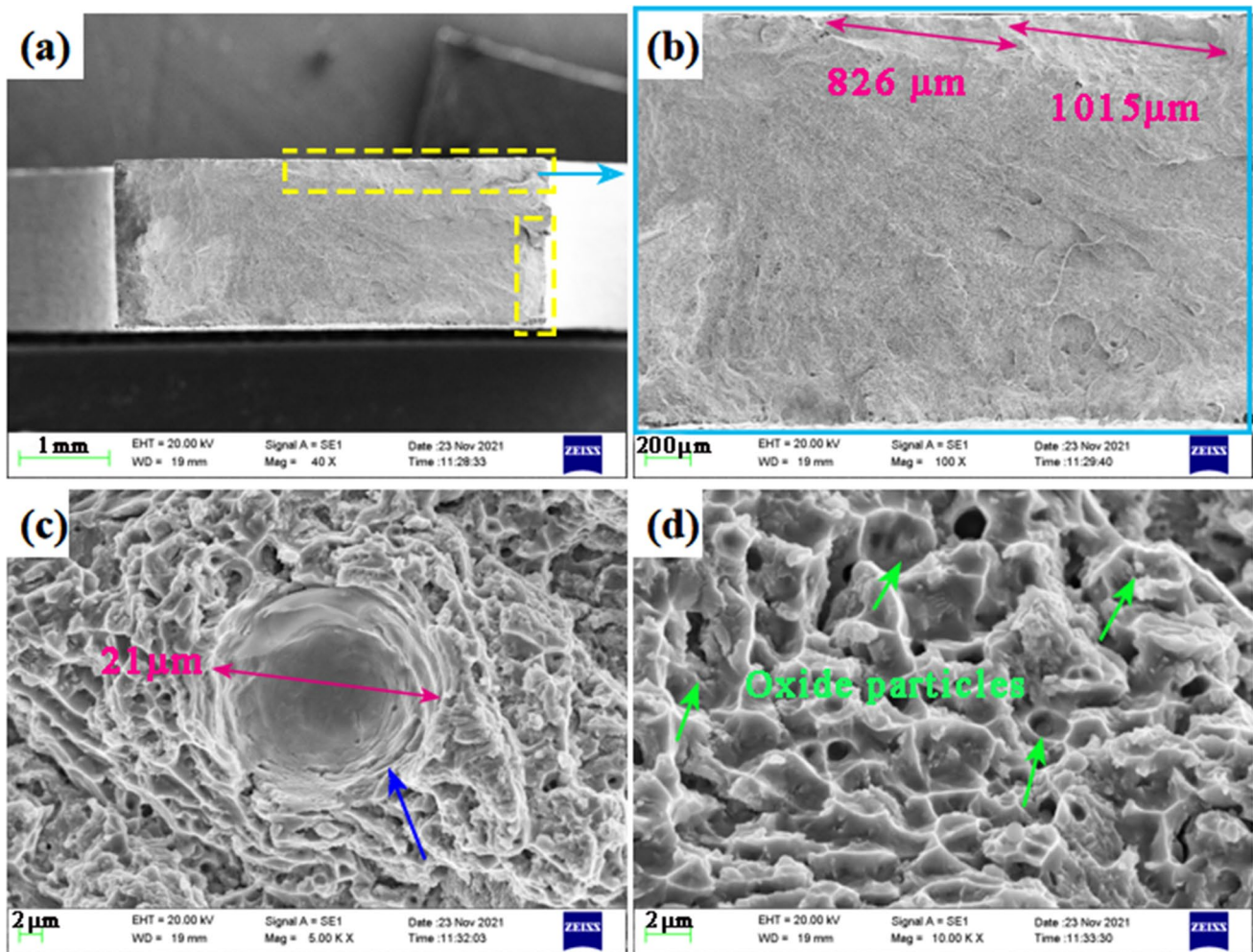


**Fig. 8** Represented fracture surface of sample ‘S2-2’ ( $\epsilon_f = 11.7\%$ ). **a** Macroscopic fracture morphology, **b** SEM image revealing the lack of fusion defects, **c** an enlarged image showing the pores, **d** a high magnified image revealing the dimple fracture and oxide particles

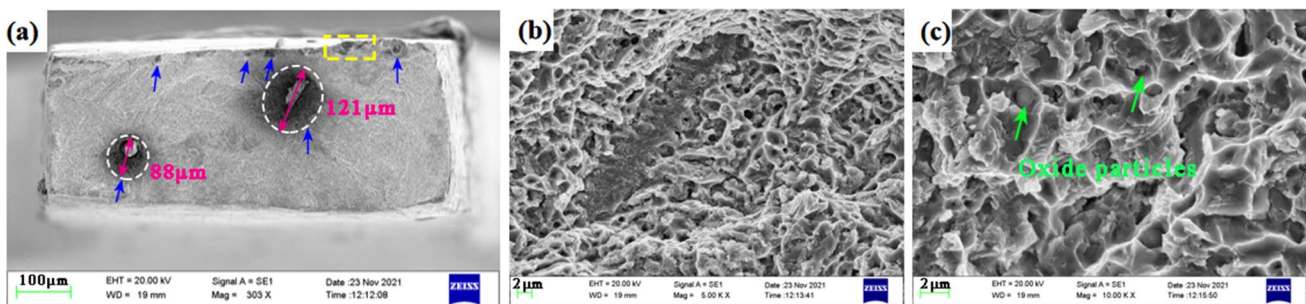


**Fig. 9** Represented fracture surface of sample ‘w4.5-4’ ( $\epsilon_f = 12.2\%$ ). **a** Macroscopic fracture morphology, **b**, **c** enlarged images showing the dimple fracture and oxide particles

[3, 8, 12, 13, 31, 38, 39]. In addition, it is observed that the tensile sample geometry (i.e., sample size and shape) has a significant impact on the elongation to failure, although microstructural variation and various types of defects

caused by the utilization of different processing parameters in these studies should also be responsible for divergent mechanical properties. Note that various testing conditions were used in the literature, namely, the utilization of

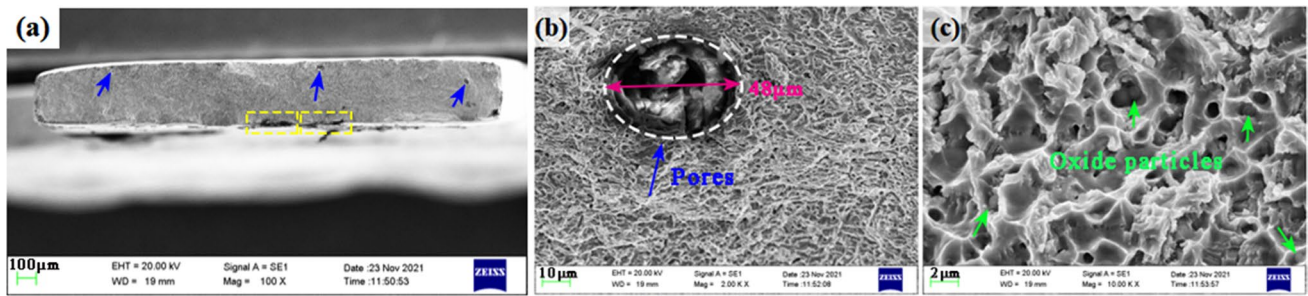


**Fig. 10** Represented fracture surface of sample ‘w10-4’ ( $\epsilon_f=15.7\%$ ). **a** Macroscopic fracture morphology, **b** SEM image revealing the pore defect, **c** a high magnified image revealing the dimple fracture and oxide particles

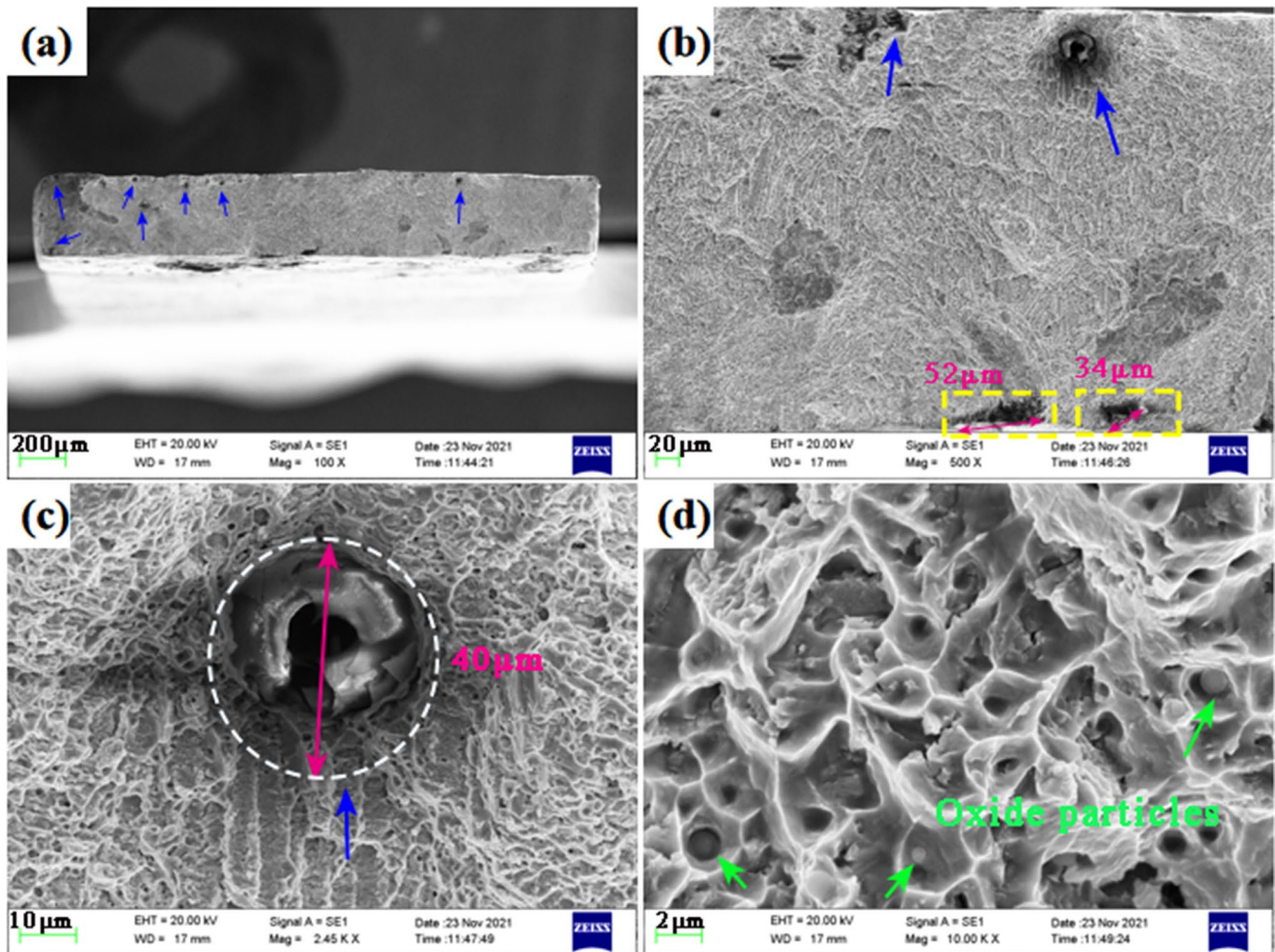


**Fig. 11** Represented fracture surface of sample ‘w10-1’ ( $\epsilon_f=35\%$ ). **a** Macroscopic fracture morphology, **b**, **c** are enlarged images showing the pores and lack of fusion defects, **d** a high magnified image revealing the dimple fracture and oxide particles

different processing parameters, printing machines, and tensile strain rates, etc., and all of these factors could affect the final mechanical properties of the samples (see Supplementary Materials, Appendix E). The various influencing factors impede us for analyzing the size effect although the

tensile specimen size may be a key reason for divergent results reported in literature. Therefore, building a correlation between elongation to failure and slimmness ratio is difficult, and further analysis by adopting the data listed in Fig. 14 was not carried out in this study.



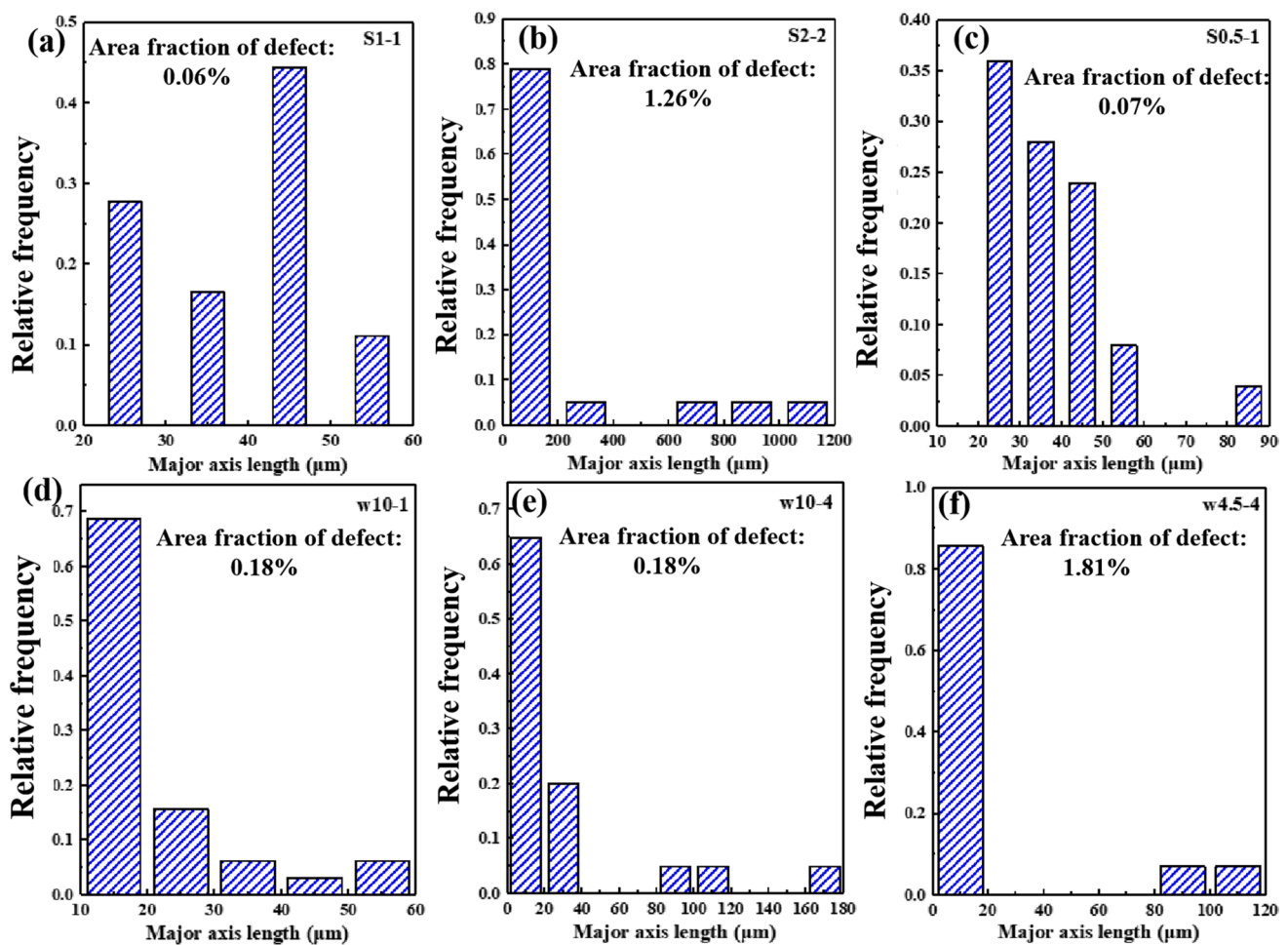


**Fig. 12** Defect size distribution measured on the observed fracture surfaces. The corresponding area fraction of defect region is also presented. **a** Sample 'S1-1', **b** Sample 'S2-2', **c** Sample 'S0.5-1', **d** Sample 'w10-1', **e** Sample 'w10-4', **f** Sample 'w4.5-4'

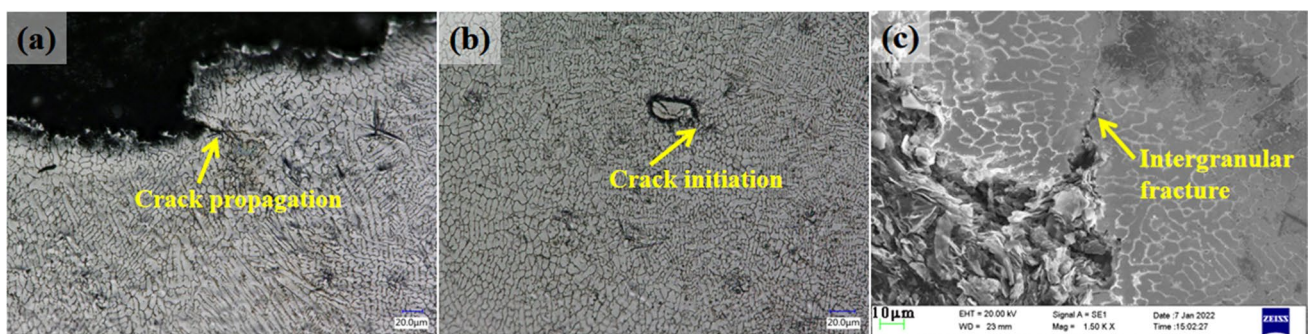


**Fig. 13** OM and SEM images showing a representative side view of LMD-produced specimen after tensile testing: **a** OM image showing the crack propagates to the edge of fractured sample surface, **b** OM image showing the crack initiates from the pore, **c** SEM image showing an intergranular fracture mode

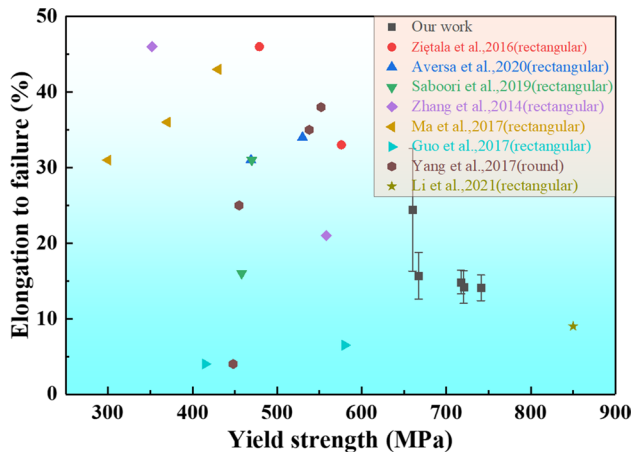
### 3.3 Microstructure Evolution After Plastic Deformation

To investigate the possible fracture mechanism and the

microstructure evolution after plastic deformation, the deformed sample was observed by SEM and EBSD, as illustrated in Figs. 13c and 15. An intergranular fracture mode was observed for such an alloy produced by LMD

**Table 3** EDS analysis results of oxide particles and LMD-produced 316L base from different sample fracture surfaces (wt%)

Spectrum location	Element					
	Si	Cr	Mn	Fe	Ni	Mo
Oxide particles	$10.80 \pm 1.61$	$27.11 \pm 4.39$	$5.59 \pm 2.93$	$45.25 \pm 4.68$	$7.50 \pm 1.00$	$2.36 \pm 1.66$
316L base material	$0.58 \pm 0.37$	$20.68 \pm 1.82$	$0.60 \pm 0.32$	$64.53 \pm 2.87$	$10.78 \pm 2.19$	$2.48 \pm 1.35$

**Fig. 14** A summary of yield strength versus elongation to failure for LMD-produced 316L SS from our work and previous studies [5, 7, 9, 14, 16–19]. The reported values are collected from different references where the LMD-produced samples are produced by different processing parameters and are tensile tested by various sample sizes and shapes

(see Fig. 13c). We have revealed that the dendrite cell boundaries, which are a kind of LAGBs, are heavily strain localized at the as-built state (Fig. 4e). However, the location of high stress status changes to HAGBs after plastic deformation (Figs. 15, 16b, d). One reason for this behavior might be the fact that the blocking ability of the dendrite cell boundaries is weaker than that of grain boundaries in terms of the strengthening effect [40]. As seen in Fig. 13, the dendrite cells remain relatively stable after deformation and are almost unchanged compared with that of the LMD-produced sample (see Fig. 3c–e), possibly due to the low ductility observed in the study. This is also evidenced by the band contrast mapping and misorientation angle distribution map shown in Fig. 15b and f that the deformed sample is still dominated by LAGBs. The role of the pre-existing high density of dislocations inside dendrite cell boundaries is to retain dislocations and offer a progressive work hardening mechanism [8, 51]. Another reason might be that the hetero-deformation induced (HDI) hardening rate caused by dendrite cell boundary was lower than that of the grain boundary determined by HAGBs [40]. It is reported that there is high HDI stress in heterogeneous material during tensile plastic deformation [52–54]. The microstructural heterogeneity can lead to dramatic strength differences in different domains, thus GND and strain partitioning are

produced to accommodate strain gradient near the various domain interfaces. However, Zhu et al. [55] pointed out that GND near the LAGBs does not produce long-range internal stress, i.e., HDI stress. Therefore, the accommodation ability of GND at the LAGBs is weaker compared with that of grain boundaries. It is widely reported that additive manufactured 316L sample is a unique heterogeneous material with their microstructural length scales spanning nearly six orders of magnitude [5, 8, 15, 35]. Hence, a high stress status near the HAGBs is observed in the deformed sample (see Fig. 16b and d). One interesting feature observed in this study is that body-centered cubic (BCC)  $\delta$  ferrite phase is formed in deformed sample (Figs. 15g and 16c). The fraction of BCC ferrite phase can be up to 2.6% (Fig. 16c). A recent work carried out by Shiao et al. argued that BCC ferrite should be  $\alpha'$  martensite in the analysis software due to the low carbon composition in the 316L SS [42]. This result suggests that austenite-to-martensite phase transformation occurs during tensile deformation of a LMD-produced 316L SS. In addition, we also noticed a significant refinement of grain size near the fracture site in the deformed sample (see Fig. 15c). The average grain size of deformed sample is  $25.43 \pm 20.83 \mu\text{m}$ , which is only 66% of the LMD-produced sample (the average grain size for LMD-produced sample is  $38.29 \pm 24.45 \mu\text{m}$ , Fig. 4h). This suggests that dynamic refinement of grain size occurs in the process of tensile plastic deformation in a LMD-produced 316L sample. The formation of refined grains might be related to the high strain localization caused by microstructure inhomogeneity or deformation incompatibility [56]. Therefore, the refinement of grain size and austenite-to-martensite phase transformation during plastic deformation should also be responsible for the excellent tensile yield strength achieved in the study (see Fig. 14).

## 4 Conclusions

In the present study, the effects of defects and specimen size on tensile properties of additively manufactured 316L SS samples produced by laser metal deposition technology were investigated. The microstructure and fracture morphology of LMD-produced samples were also inspected. The obtained tensile properties accordingly to various sample sizes were compared to previously published works. The major findings are summarized as follows:



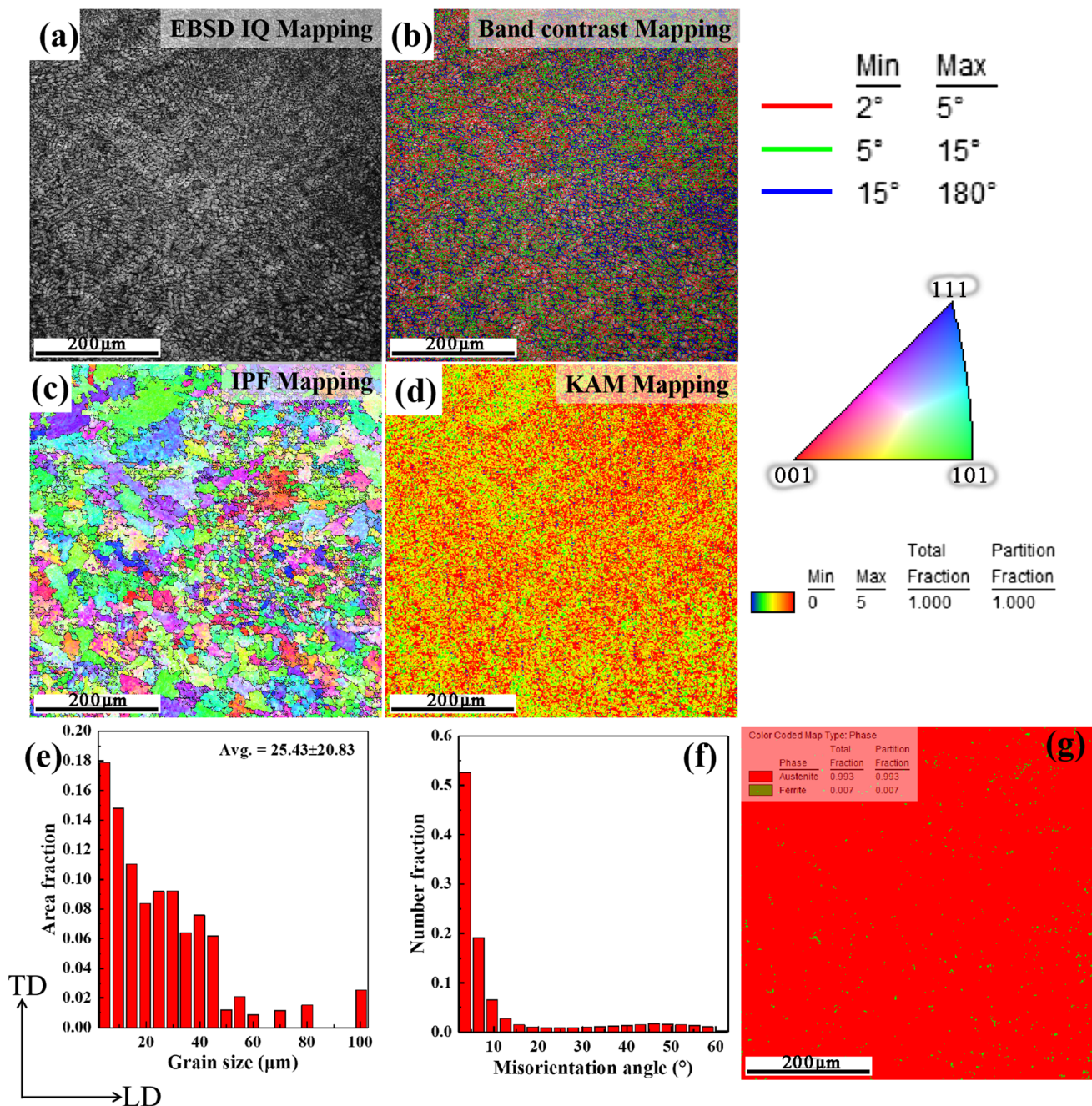


**Fig. 15** Microstructures of deformed sample: **a** IQ map, **b** band contrast map, **c** IPF image, **d** KAM map, **e** grain size distribution, **f** misorientation angle distribution, **g** phase mapping

1. The microstructure of the LMD-produced 316L SS consists of columnar dendrites and cellular structures with an average grain size of 38.29  $\mu\text{m}$  and dendrite spacing of 2–5  $\mu\text{m}$ , respectively. In addition, grain boundaries of LMD-produced samples are decorated with a fraction of 38.7% LAGBs where the highest stress status is located in these boundaries. However, the location of high stress status changes to HAGBs after the LMD-produced sample subjected to plastic deformation.
2. The tensile tested specimen size has a pronounced effect on mechanical properties of LMD-produced samples, especially when the non-standard miniature-sized specimens are used. The YS and UTS values might be underestimated when a miniature-sized specimen is adopted, while the variation of  $\epsilon_f$  values exhibits a direct correlation with the slimness ratio.
3. The cluster of pores and occupancy location of lack of fusion defects play a significant role in determining the



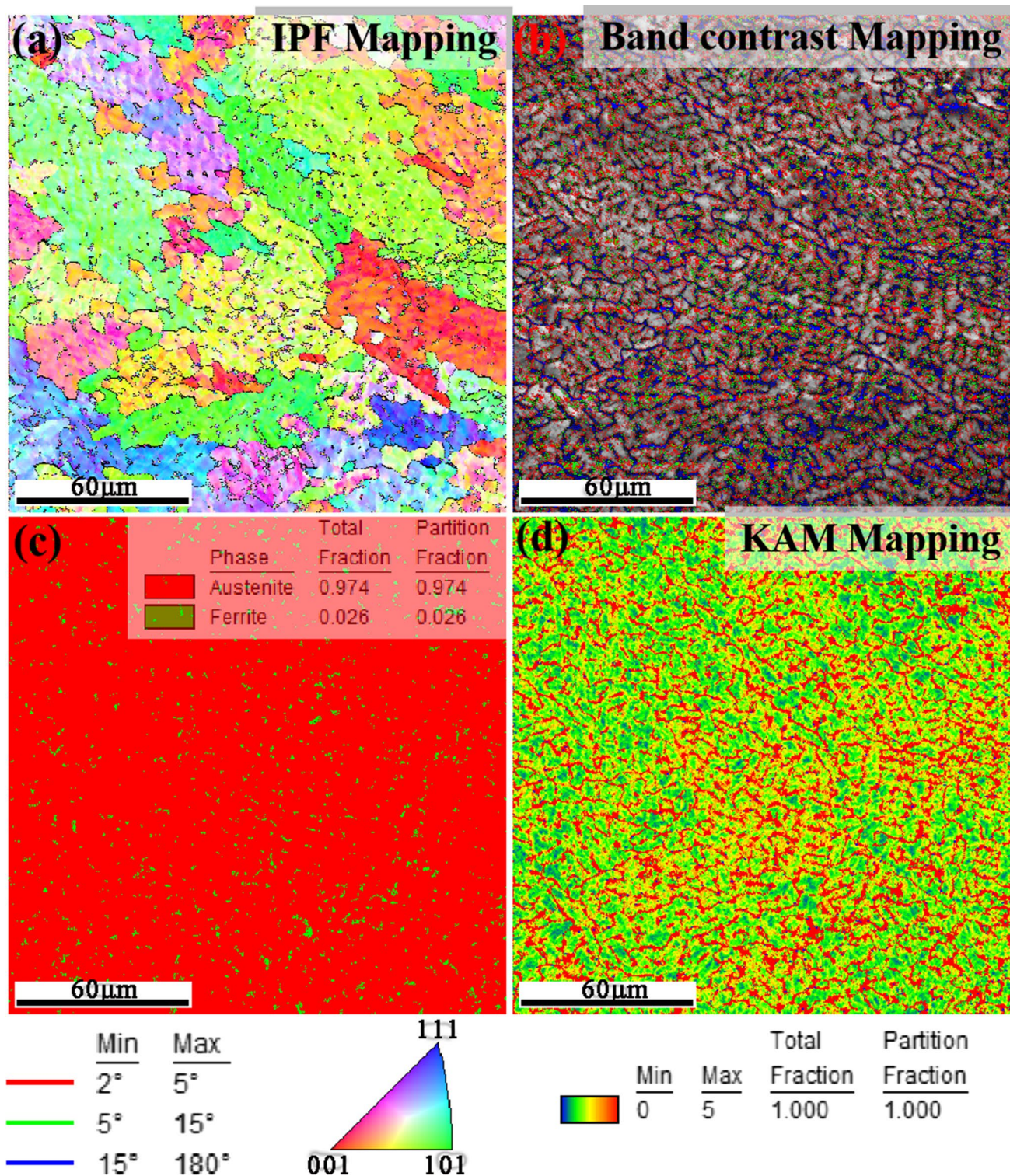


**Fig. 16** A magnified image of deformed sample observed in another area: **a** IPF image, **b** band contrast map, **c** phase mapping, **d** KAM map

ductility of LMD-produced 316L SS samples. These two kinds of defects can not only act as a stress amplifier which in turn accelerates crack propagation during tensile loading, but also cause a reduction of effective

cross-sectional area, both of which results in a decreased elongation to failure.

4. Compared with a conventionally manufactured counterpart and those data reported in previous studies,



very high UTS and YS values were obtained in the current study which are 660–741 MPa and 879–938 MPa, respectively. Whilst, the values of elongation to failure were relatively lower, with an average value ranged between 14.1 and 24.4% depending on the adopted tensile specimen size. Despite the unique hierarchically heterogeneous microstructure formed in LMD-produced samples, the refinement of grain size and austenite-to-martensite phase transformation during plastic deformation should also be responsible for the excellent tensile yield strength achieved in the study.

**Supplementary Information** The online version contains supplementary material available at <https://doi.org/10.1007/s40195-022-01445-z>.

**Acknowledgements** This work was financially supported by the National Natural Science Foundation of China (Grant No. 11772344). The authors acknowledge engineer Bao-Chun Cai for his experimental assistance during the performance of tensile test.

## Declarations

**Conflict of interest** The authors state that there are no conflicts of interest to disclose.

## References

- [1] D. Svetlizky, M. Das, B. Zheng, A.L. Vyatsikh, S. Bose, A. Bandyopadhyay, J.M. Schoenung, E.J. Lavernia, N. Eliaz, *Mater. Today* **49**, 271 (2021)
- [2] H.Z. Jiang, Z.Y. Li, T. Feng, P.Y. Wu, Q.S. Chen, Y.L. Fen, S.W. Li, H. Gao, H.J. Xu, *Opt. Laser. Technol.* **119**, 105592 (2019)
- [3] H.Z. Jiang, Z.Y. Li, T. Feng, P.Y. Wu, Q.S. Chen, Y.L. Feng, L.F. Chen, J.Y. Hou, H. Xu, *Acta Metall. Sin.* **34**, 495 (2020). (**Engl. Lett.**)
- [4] Y. Zhong, L.F. Liu, S. Wikman, D.Q. Cui, Z.J. Shen, *J. Nucl. Mater.* **470**, 170 (2016)
- [5] M. Ziętała, T. Durejko, M. Polański, I. Kunce, T. Płociński, W. Zieliński, M. Łazińska, W. Stępniewski, T. Czujko, K.J. Kurzydłowski, Z. Bojar, *Mater. Sci. Eng. A* **677**, 1 (2016)
- [6] P. Kürsteiner, M.B. Wilms, A. Weisheit, B. Gault, E.A. Jägle, D. Raabe, *Nature* **582**, 515 (2020)
- [7] N. Li, Z. Li, Y. Wei, *Nanomaterials* **11**, 2859 (2021)
- [8] Y.M. Wang, T. Voisin, J.T. McKeown, J. Ye, N.P. Calt, Z. Li, Z. Zeng, Y. Zhang, W. Chen, T.T. Roehling, R.T. Ott, M.K. Santala, P.J. Depond, M.J. Matthews, A.V. Hamza, T. Zhu, *Nat. Mater.* **17**, 63 (2018)
- [9] M. Ma, Z. Wang, X. Zeng, *Mater. Sci. Eng. A* **685**, 265 (2017)
- [10] D. Herzog, V. Seyda, E. Wycisk, C. Emmelmann, *Acta Mater.* **117**, 371 (2016)
- [11] A. Saboori, A. Aversa, G. Marchese, S. Biamino, M. Lombardi, P. Fino, *Appl. Sci. Basel* **10**, 3310 (2020)
- [12] L. Liu, Q. Ding, Y. Zhong, J. Zou, J. Wu, Y.L. Chiu, J. Li, Z. Zhang, Q. Yu, Z. Shen, *Mater. Today* **21**, 354 (2018)
- [13] Z.J. Sun, X.P. Tan, S.B. Tor, C.K. Chua, *NPG Asia Mater.* **10**, 127 (2018)
- [14] N. Yang, J. Yee, B. Zheng, K. Gaiser, T. Reynolds, L. Clemon, W.Y. Lu, J.M. Schoenung, E.J. Lavernia, *J. Therm. Spray Technol.* **26**, 610 (2017)
- [15] Z. Yan, K. Zou, M. Cheng, Z. Zhou, L. Song, *J. Mater. Res. Technol.* **15**, 582 (2021)
- [16] A. Aversa, A. Saboori, E. Librera, M. de Chirico, S. Biamino, M. Lombardi, P. Fino, *Addit. Manuf.* **34**(101274), 101274 (2020)
- [17] A. Saboori, A. Aversa, F. Bosio, E. Bassini, E. Librera, M. De Chirico, S. Biamino, D. Ugues, P. Fino, M. Lombardi, *Mater. Sci. Eng. A* **766**, 138360 (2019)
- [18] K. Zhang, S. Wang, W. Liu, X. Shang, *Mater. Des.* **55**, 104 (2014)
- [19] P. Guo, B. Zou, C. Huang, H. Gao, *J. Mater. Process. Technol.* **240**, 12 (2017)
- [20] D. Gu, X. Shi, R. Poprawe, D.L. Bourell, R. Setchi, J. Zhu, *Science* **372**, 932 (2021)
- [21] K. Mertová, J. Džugan, M. Roudnická, M. Daniel, D. Vojtěch, M. Seifi, J.J. Lewandowski, *Metals* **10**, 1340 (2020)
- [22] P. Wang, M.H. Goh, Q. Li, M.L.S. Nai, J. Wei, *Virtual Phys. Prototyp.* **15**, 251 (2020)
- [23] B. Brown, W. Everhart, J. Dinardo, *Rapid Prototyp. J.* **22**, 801 (2016)
- [24] A.M. Roach, B.C. White, A. Garland, B.H. Jared, J.D. Carroll, B.L. Boyce, *Addit. Manuf.* **32**, 101090 (2020)
- [25] J. Džugan, M. Seifi, R. Prochazka, M. Rund, P. Podany, P. Konopik, J.J. Lewandowski, *Mater. Charact.* **143**, 94 (2018)
- [26] D. Barba, C. Alabort, Y. Tang, M. Viscasillas, R. Reed, E. Alabort, *Mater. Des.* **186**, 108235 (2020)
- [27] A. Saboori, G. Piscopo, M. Lai, A. Salmi, S. Biamino, *Mater. Sci. Eng. A* **780**, 139179 (2020)
- [28] J. Shi, P. Zhu, G. Fu, S. Shi, *Opt. Laser. Technol.* **101**, 341 (2018)
- [29] W. Yang, Y. Tarng, *J. Mater. Process. Technol.* **84**, 122 (1998)
- [30] M. Ma, Z. Wang, D. Wang, X. Zeng, *Opt. Laser. Technol.* **45**, 209 (2013)
- [31] H.Z. Jiang, Z.Y. Li, T. Feng, P.Y. Wu, Q.S. Chen, S.K. Yao, J.Y. Hou, *Acta Metall. Sin. -Engl. Lett.* **35**, 773 (2021)
- [32] Z. Li, T. Voisin, J.T. McKeown, J.C. Ye, T. Braun, C. Kamath, W.E. King, Y.M. Wang, *Int. J. Plasticity* **120**, 395 (2019)
- [33] T. Debroy, H.L. Wei, J.S. Zuback, T. Mukherjee, J.W. Elmer, J.O. Milewski, A.M. Beese, A. Wilson-Heid, A. De, W. Zhang, *Prog. Mater. Sci.* **92**, 112 (2018)
- [34] J. Li, D. Deng, X. Hou, X. Wang, G. Ma, D. Wu, G. Zhang, *Mater. Sci. Technol.* **32**, 1223 (2016)
- [35] B. Barkia, P. Aubry, P. Haghi-Ashtiani, T. Auger, L. Gosmain, F. Schuster, H. Maskrot, *J. Mater. Sci. Technol.* **41**, 209 (2020)
- [36] T. Kurzynowski, K. Gruber, W. Stopyra, B. Kuźnicka, E. Chlebus, *Mater. Sci. Eng. A* **718**, 64 (2018)
- [37] A. Yadollahi, N. Shamsaei, S.M. Thompson, D.W. Seely, *Mater. Sci. Eng. A* **644**, 171 (2015)
- [38] M. Shamsujjoha, S.R. Agnew, J.M. Fitz-Gerald, W.R. Moore, T.A. Newman, *Metall. Mater. Trans. A* **49**, 3011 (2018)
- [39] D. Kong, C. Dong, X. Ni, L. Zhang, J. Yao, C. Man, X. Cheng, K. Xiao, X. Li, *J. Mater. Sci. Technol.* **35**, 1499 (2019)
- [40] D. Kong, C. Dong, X. Ni, Z. Liang, C. Man, X. Li, *Mater. Res. Lett.* **8**, 390 (2020)
- [41] M. Mukherjee, *Materialia* **7**, 100359 (2019)
- [42] C.-H. Shiao, M.D. McMurtrey, R.C. O'Brien, N.D. Jerred, R.D. Scott, J. Lu, X. Zhang, Y. Wang, L. Shao, C. Sun, *Mater. Des.* **204**, 109644 (2021)
- [43] J.W. Elmer, S.M. Allen, T.W. Eagar, *Metall. Mater. Trans. A* **20**, 2117 (1989)
- [44] I. Tolosa, F. Garciandía, F. Zubiri, F. Zapirain, A. Esnaola, *Int. J. Adv. Manuf. Technol.* **51**, 639 (2010)
- [45] I.A. Segura, L.E. Murr, C.A. Terrazas, D. Bermudez, J. Mireles, V.S.V. Injeti, K. Li, B. Yu, R.D.K. Misra, R.B. Wicker, *J. Mater. Sci. Technol.* **35**, 351 (2019)
- [46] C. Elangesswaran, A. Cutolo, G.K. Muralidharan, C. de Formanoir, F. Berto, K. Vanmeensel, B. Van Hooreweder, *Int. J. Fatigue* **123**, 31 (2019)
- [47] T.M. Mower, M.J. Long, *Mater. Sci. Eng. A* **651**, 198 (2016)

- [48] J. R. Davis, Tensile testing, 2nd edn. (ASM International, United States of America, 2004), pp. 45–46.
- [49] K. Saeidi, L. Kvetkova, F. Lofajc, Z.J. Shen, RSC Adv. **5**, 20747 (2015)
- [50] L. Cui, S. Jiang, J. Xu, R.L. Peng, R.T. Mousavian, J. Moverare, Mater. Des. **198**, 109385 (2021)
- [51] T. Voisin, J.B. Forien, A. Perron, S. Aubry, N. Bertin, A. Samanta, A. Baker, Y.M. Wang, Acta Mater. **203**, 116476 (2021)
- [52] X. Wu, Y. Zhu, Mater. Res. Lett. **5**, 527 (2017)
- [53] X. Wu, M. Yang, F. Yuan, G. Wu, Y. Wei, X. Huang, Y. Zhu, P. Natl. Acad. Sci. USA **112**, 14501 (2015)
- [54] J. He, Y. Ma, D. Yan, S. Jiao, F. Yuan, X. Wu, Mater. Sci. Eng. A **726**, 288 (2018)
- [55] Y. Zhu, X. Wu, Mater. Res. Lett. **7**, 393 (2019)
- [56] C. Sun, W. Chi, W. Wang, Y. Duan, Int. J. Mech. Sci. **205**, 106591 (2021)

Springer Nature or its licensor holds exclusive rights to this article under a publishing agreement with the author(s) or other rightsholder(s); author self-archiving of the accepted manuscript version of this article is solely governed by the terms of such publishing agreement and applicable law.